

# Modeling and Real-Time Cartesian Impedance Control of 3-DOF Robotic Arm in Contact with the Surface

Ayberk Beyhan<sup>1</sup>, Nurettin Gökhan Adar<sup>1\*</sup>

<sup>1</sup>Department of Mechatronics Engineering, Faculty of Engineering and Natural Sciences, Bursa Technical University, 16310 Bursa, Turkey

\*. Corresponding author.

Tel.:

E-mail address: gokhan.adar@btu.edu.tr (N.G.Adar)

21261344001@ogrenci.btu.edu.tr (A.Beyhan)

## Abstract

Robotic arms have become increasingly popular and widely used in various industrial applications. However, conventional control methods are not capable of adequately controlling a robotic arm in tasks that require contact with a surface. To address this issue, this study proposes a Cartesian impedance control method to control a 3-DOF robotic arm in real-time during contact with a surface. The proposed controller consists of two control loops: an inner loop and an outer loop. The inner loop utilizes a motion control method in the joint space, with the parameters of the controller being calculated through system identification. The outer loop implements Cartesian impedance control in the Cartesian space using a mass-spring-damper model. The coefficients of the Cartesian impedance control were determined based on the over-damped response with real-time applications. By selecting the inner loop in the joint space and the outer loop in the Cartesian space, the control of the robotic arm is guaranteed. The proposed method was tested in real-time, and its performance was compared with the PID with gravity compensation control in the Cartesian space. The results indicated that the proposed method was able to successfully follow reference trajectories and reduce the contact force.

**Keywords:** Cartesian impedance control, Robotic arm, Position control, PID with gravity compensation, Real-time control.

## 1. Introduction

Robotic arms are widely adopted in various industries, including assembly, handling, picking, painting, and packaging, among others. Many control algorithms have been developed and implemented to control the robotic arm without contact with its environment. On the other hand, when contact occurs between the robotic arm and the environment, its control and manipulation are difficult and complex. It is necessary to include Force Control to overcome contact problems. Force control adapts the forces generated by the contact and enables them to be reliably controlled so that the robotic arm can interact safely with the environment.

Force control is divided into two main categories as direct and indirect force control methods. Stiffness control, impedance control, and admittance control are the most well-known indirect force control methods [1]. The most known and researched indirect force control method is the impedance control method first introduced by Hogan [2]. Impedance control is categorized into three subparts which are Dynamic-Based Impedance Control (DB-IC), Position-Based Impedance Control (PB-IC) [3–6], Instantaneous-Model-Based Impedance Control [7]. DB-IC relies heavily on robot dynamics. Therefore, the controller is sensitive to modeling errors [8,9].

Cartesian Impedance Control (C-IC) is a variation of PB-IC where the robot's motion is controlled in the Cartesian space rather than in the joint space. It is a method of controlling the movement of a robotic arm in a way that the robotic arm behaves like a system with compliant properties. One of the main reasons for using C-IC is to provide stability during interactions with the environment. C-IC allows the robotic arm to respond to external forces in a predictable and stable manner, enabling more precise and accurate control of its movement.

Additionally, C-IC allows for more natural and intuitive human-robot interactions. It also provides a way to control the robot's motion and interactions with the environment in a way that is independent of the robot's internal configuration. This makes the control system more robust to changes in the robot's internal structure or kinematics.

Compared to other control methods, C-IC offers several advantages. It is simple to implement, easy to understand and it can also be used for motion planning, force control, and collision avoidance.

In the literature, numerous studies have demonstrated the effectiveness of impedance control in simulations involving a wide range of robot types and degrees of freedom. C-IC was implemented in a two-link planar robotic arm. While the robot's joints were controlled by Computed Torque Control, the impedance control compensated for the interaction force in Cartesian space [10]. Hybrid position and force control were proposed for the PUMA 560 robot. The target force was set so that the robot operated accurately during contact [11]. A mobile robot equipped with 3 DOF robotic arm was designed for pipe repair tasks. Since the robot would come into contact with the pipe while performing a repair task, impedance control was chosen to precisely control the robotic arm. The simulation results showed that the robotic arm could successfully follow the trajectory even in contact with the environment [12]. A ROS simulation platform for dual-arm mobile manipulation was proposed to perform impedance control. Simulation results for both the navigation and manipulation of the dual-arm mobile platform demonstrated the compatibility of the simulator [13]. The proximity sensor was adopted to prevent a collision when performing another impedance control simulation. The simulation results showed the robot works more safely and accurately thanks to the sensor [14]. Two-arm manipulator was integrated with impedance control to compensate for the contact reactions when the end effector touches the target body [15]. Free-floating manipulator was simulated with C-IC for space missions [16].

UR16e Universal-Robot and the haptic device were adapted to teleoperate live-line maintenance and velocity-based impedance control was implemented for both the robot-environment and robot-haptic device. The experimental setup was built to remove the coating off cables. Remarkably accurate force and motion control were obtained in real-time [17]. The KUKA LBR7 R800 industrial robot was equipped with tools for various tasks while the robot tool was operated by a human. Numerical and experimental studies for impedance control were applied and results were given in graphs for autonomous and collaborative interaction [18]. Computed torque impedance control was performed for mold polishing and mold surface finishing in the collaborative application [19,20]. C-IC was implemented for the Franka Emika Panda robotic arm. Experimental results for Locomotion, Manipulation, and Loco-Manipulation validated the proposed method [21]. An online scalable tele-impedance framework was developed for multi-robot teleoperation in a medical application. It has a simple interface that realizes individual and collaborative control of three different experiments as a mock-up patient, a cooperative task, and

a collaborative task [22]. UR5e that was controlled with impedance control was conducted for the task of inserting automatic charging gun [23]. Studies on the implementation of impedance control for robotic hands also are being carried out to cope with the contact force [4,24]. As technology advances, robotic devices are becoming increasingly prevalent in the healthcare industry. Since these devices are expected to be both accurate and precise, impedance control applications are implemented in surgeries [25–27], rehabilitation [28–30], and surgical devices [31].

In this study, Cartesian impedance control is proposed for a low-cost robotic arm that is in contact with the surface. The proposed control algorithm for the low-cost robotic arm aims to achieve a robust control structure by combining two control loops, the inner loop, and the outer loop. The inner loop is comprised of a motion control, which uses a PID with gravity compensation, to control the robotic arm in the joint space. The outer loop is a Cartesian impedance control, which is designed to compensate for the reaction forces that occur during contact with the surface.

The PID with gravity compensation which is applied in this study considers not only the joint position but also the joint velocity, which enhances the control performance of the robotic arm. Additionally, the algorithm includes gravity compensation in its motion control, which helps to account for the effects of gravity on the robotic arm and improves its stability. In this way, the combination of the Cartesian impedance control and the motion control creates a robust control structure that guarantees control of the robotic arm in both the Cartesian and joint spaces.

The proposed control method has been also compared with a conventional PID with gravity compensation in terms of real-time control of the robotic arm during contact with the surface. The comparison results show that the proposed control algorithm provides better performance in terms of tracking the desired trajectory and compensating for the reaction forces during contact.

The results showed that the proposed control algorithm for the low-cost robotic arm is a promising solution for robotic arm control, as it relies only on force sensing for Cartesian impedance control and considers both joint position and velocity, as well as gravity compensation for motion control.

## 2. Kinematics of 3-DOF Robotic Arm

The forward kinematics equations of the robotic arm were obtained using the Modified Denavit Hartenberg (D-H) method [32]. The frames given in Figure 1 were attached to the joints according to the modified D-H method.

The D-H table was constructed using each neighborhood frame as shown in Table 1.

In this convention, each homogeneous transformation is represented as follow:

$${}^{n-1}T_n = \begin{bmatrix} c\theta_i & -s\theta_i & 0 & a_{i-1} \\ s\theta_i c\alpha_{i-1} & c\theta_i c\alpha_{i-1} & -s\alpha_{i-1} & -s\alpha_{i-1}d_i \\ s\theta_i s\alpha_{i-1} & c\theta_i s\alpha_{i-1} & c\alpha_{i-1} & c\alpha_{i-1}d_i \\ 0 & 0 & 0 & 1 \end{bmatrix} \quad (1)$$

The homogeneous transformation matrices between each neighborhood frame were calculated using Table 1 as follows:

$${}^0_1T = \begin{bmatrix} c\theta_1 & -s\theta_1 & 0 & 0 \\ s\theta_1 & c\theta_1 & 0 & 0 \\ 0 & 0 & 1 & l_1 \\ 0 & 0 & 0 & 1 \end{bmatrix} \quad (2)$$

$${}^1_2T = \begin{bmatrix} c\theta_2 & -s\theta_2 & 0 & 0 \\ 0 & 0 & -1 & 0 \\ s\theta_2 & c\theta_2 & 0 & 0 \\ 0 & 0 & 0 & 1 \end{bmatrix} \quad (3)$$

$${}^2_3T = \begin{bmatrix} c\theta_3 & -s\theta_3 & 0 & l_2 \\ s\theta_3 & c\theta_3 & 0 & 0 \\ 0 & 0 & 1 & 0 \\ 0 & 0 & 0 & 1 \end{bmatrix} \quad (4)$$

$${}^3_4T = \begin{bmatrix} 1 & 0 & 0 & l_3 \\ 0 & 1 & 0 & 0 \\ 0 & 0 & 1 & 0 \\ 0 & 0 & 0 & 1 \end{bmatrix} \quad (5)$$

Position and orientation of end effector with respect to Frame 0 was computed by multiplying each transformation matrices and  ${}^0_4T$  was given respectively.

$${}^0_4T = {}^0_1T {}^1_2T {}^2_3T {}^3_4T \quad (6)$$

$${}^0_4T = \begin{bmatrix} c\theta_1 c\theta_{23} & -c\theta_1 s\theta_{23} & s\theta_1 & c\theta_1 (l_2 c\theta_2 + l_3 c\theta_{23}) \\ s\theta_1 c\theta_{23} & -s\theta_1 s\theta_{23} & -c\theta_1 & s\theta_1 (l_2 c\theta_2 + l_3 c\theta_{23}) \\ s\theta_{23} & c\theta_{23} & 0 & l_1 + l_2 s\theta_2 + l_3 s\theta_{23} \\ 0 & 0 & 0 & 1 \end{bmatrix} \quad (7)$$

In this study, the robot's inverse kinematics equations were calculated using the geometric solution approach [33]. The position of the end effector of the robotic arm and the variables were given in Cartesian space and shown in Figure 2.

The rotation of the robot around the z-axis occurs with respect to  $\theta_1$  was calculated using  $p_x$  and  $p_y$  coordinates of the end effector.

$$\theta_1 = \tan^{-1} \left( \frac{p_y}{p_x} \right) \quad (8)$$

The auxiliary lengths of the triangle ( $r_1$ ,  $r_2$  and  $r_3$ ) were calculated as:

$$r_1 = \sqrt{p_x^2 + p_y^2} \quad (9)$$

$$r_2 = p_z - d_1 \quad (10)$$

$$r_3 = \sqrt{r_1^2 + r_2^2} \quad (11)$$

Using the tangent trigonometric function,  $\varphi_2$  was:

$$\varphi_2 = \tan^{-1} \left( \frac{r_2}{r_1} \right) \quad (12)$$

$\varphi_3$  and  $\varphi_1$  were obtained Using the Cosine theorem in triangle.

$$\varphi_3 = \cos^{-1} \left( \frac{-r_3^2 + l_2^2 + l_3^2}{2l_2 l_3} \right) \quad (13)$$

$$\varphi_1 = \cos^{-1} \left( \frac{-l_3^2 + l_2^2 + r_3^2}{2l_2r_3} \right) \quad (13)$$

The second and third links formed a 2 DOF planar robot. Relation between  $\varphi_1$ ,  $\varphi_2$ ,  $\varphi_3$  and  $\theta_2$ ,  $\theta_3$  are given as:

$$\theta_2 = \varphi_2 - \varphi_1 \quad (14)$$

$$\theta_3 = \varphi_3 - 180 \quad (15)$$

### 3. Real Time Implementations

This study presents an experimental setup designed to evaluate the performance of the proposed control algorithms which are divided into two sections. The first section is focused on the analysis and implementation of PID with Gravity Compensation Control, while the second section is dedicated to the investigation of C-IC, which is the primary topic of the study.

The experimental setup comprises of a computer, an Arduino Mega2560 microcontroller, a power supply, VNH 5019 motor controller and a robotic arm that is equipped with a force sensor, as depicted in Figure 3. Arduino Mega2560 establishes the connection between computer, motors and force sensor. The real-time experiments executed with Matlab/Simulink.

#### 3.1 Motion Control

PID control is a classical control method that is widely used in various control systems, including robotics. It aims to eliminate the error between the desired and the actual system output by using its coefficients, P, I and D. PID control is a closed-loop control system that uses feedback to control the system (Figure 4).

The mathematical model of PID control is given as:

$$u = K_P(q_d - q) + K_I \int ((q_d - q))dt + K_D(\dot{q}_d - \dot{q}) \quad (16)$$

where  $K_P$ ,  $K_I$ , and  $K_D$  are the PID coefficients,  $q_d$ ,  $\dot{q}_d$  desired joint angle/velocity,  $q$  and  $\dot{q}$  present joint angle/velocity,  $u$  is control input.

PID control does not ensure stable control of the robotic arm as it operates under gravity fields. To balance the gravitational torques, PID with Gravity Compensation Control is selected for motion control. The block diagram of the controller is given in Figure 5.

In Figure 5,  $P_d$  represents the x,y,z position of the end-effector of the robotic arm. In order to control the robotic arm's movement, the x-y-z position must be converted into the angle of each joint. This is because robotic arms are controlled in joint space, not in Cartesian space (x-y-z coordinates).

Inverse kinematics is used to transform the desired end-effector position in Cartesian space (x, y, z coordinates) into the corresponding joint angles required to achieve that position.

Adding a gravity term to the PID control compensates for the effects of gravity on a system, resulting in a PID with gravity compensation.

The mathematical model of the controller is given as:

$$u = K_P(q_d - q) + K_I \int ((q_d - q))dt + K_D(\dot{q}_d - \dot{q}) + G(q)K_G \quad (17)$$

where  $G(q)$  is the gravitational torque.  $K_G$  is a gain and is calculated as the ratio of input voltage and torque value.

The gravitational torques for the second and third links that operated against the gravitational fields were calculated as follows:

$$g_2 = \square_3 m_3 g \cos(\theta_2 + \theta_3) + l_2 m_3 g \cos \theta_2 + \square_2 m_2 g \cos \theta_2 \quad (18)$$

$$g_3 = \square_3 m_3 g \cos(\theta_2 + \theta_3) \quad (19)$$

where  $m_2$  and  $m_3$  are the weight of the second and third links and  $h_2$  and  $h_3$  are the height of the center of gravity of the second and third links.

Due to the difficulty and complexity of the dynamics of the robotic arm, system identification was applied to create a mathematical model of the robotic arm. The mathematical model of each link coupled with the motor was estimated with the Matlab System Identification toolbox [34].

The input data for the mathematical model of each link coupled with the motor was the motor voltage, while the output data was the angular position of the link. Figure 6 provides an illustration of the input and output data for the first link.

The transfer function, which describes the relationship between the input and output of a system, was estimated for different poles and zeros. These results were then compared in Figure 7 to evaluate the performance of the system.

The two poles, one zero transfer function was chosen as the best fit among the estimated transfer functions for the first link. The reason for this choice is that it was the best representation of the system dynamics.

The transfer function of the first link is obtained as:

$$\frac{\theta_1(s)}{V_1(s)} = \frac{-0.148s + 4.846}{s^2 + 9.675s + 5.033 \times 10^{-13}} \quad (20)$$

where,  $\theta_1$  is output angle and  $V_1$  is the input voltage for the first link.

The closed-loop transfer function of a system with a PID controller can be derived using the transfer function of the robotic arm and the transfer function of the PID controller. The resulting transfer function represents the relationship between the output and the input of the closed-loop system:

$$\frac{\theta_1(s)}{P_{d1}(s)} = \frac{-0.15K_d s^3 + a s^2 + b s + 4.8K_i}{(1 - 0.15K_d)s^3 + (a + 9.7)s^2 + b s + 4.8K_i} \quad (22)$$

$$a = (4.8K_d - 0.15K_p)$$

$$b = (4.8K_p - 0.15K_i)$$

$P_{d1}$  is desired x-y-z Cartesian vector for the first link.

When tuning the coefficients of a PID controller, it is important to ensure that the closed-loop system remains stable. The Routh-Hurwitz criteria was used to evaluate the stability of the system for PID coefficients, and the parameters were obtained and was given in Table 2.

Considering the stability criteria found by Routh-Hurwitz stability analysis, the PID coefficients were chosen to satisfy the conditions such as Overshoot, settling time, and rise time. Figure 8 shows a white region where the closed-loop response of each joint can be selected if overshoot is below 5%, settling time is below 1 second, and rise time is below 0.1 seconds.

The poles for the robotic arm were desired on the x-axis to achieve an overdamped system response, and the PID coefficients for each joint were calculated based on these poles. Desired eigenvalues were chosen  $s_1 = -0.23$ ,  $s_2 = -5.4$ ,  $s_3 = -16.5$  and then the desired characteristic equation became for the first link as:

$$s^3 + \frac{(a+9.7)}{1-0.15k_d}s^2 + \frac{b}{1-0.15k_d}s + \frac{4.8k_i}{1-0.15k_d} = s^3 + 20.25s^2 + 205s + 50 \quad (21)$$

The same design procedure was repeated for the second and third links, and the resulting PID coefficients for all three links are listed in Table 3.

To evaluate the performance of the controller in real-time experiments, reference trajectories in the joint space were chosen as defined by Equation 24. As illustrated in Figure 9, the results indicate that the control algorithm was able to effectively follow the reference trajectory.

$$\begin{aligned} \theta_1(t) &= 0.088t^3 - 0.008t^4 + 0.0002t^5 \\ \theta_2(t) &= -0.088t^3 + 0.008t^4 - 0.0002t^5 \\ \theta_3(t) &= 0.088t^3 - 0.008t^4 + 0.0002t^5 \end{aligned} \quad (24)$$

### 3.2 Cartesian Impedance Control

When a robotic arm comes into contact with an object, the motion of the robotic arm is affected by the forces exerted by the object on the robotic arm, and the system becomes a closed-loop one. In this case, PID control is not sufficient because it does not take into account the dynamic properties of the environment and the robotic arm's resistance to motion.

C-IC, on the other hand, is better suited for closed-loop systems because they take into account the robotic arm's contact force and the dynamic properties of the environment. This method allows the robotic arm to react to external forces in a compliant manner, which is crucial when the robotic arm is in contact with an object.

C-IC is a control method used in the robotic arm that combines the inner loop of PID with gravity compensation and the outer loop of C-IC. The inner loop uses PID with gravity compensation to accurately track the desired position of the robotic arm, while the outer loop uses C-IC to provide a compliant and stable interaction with the environment. This allows the robotic arm to respond to external forces naturally and stably, while still achieving precise positioning. The parameters of the PID with gravity compensation controller calculated in section 3.1 were carried out. The block diagram of the C-IC was illustrated in Figure 10.

In C-IC, the relationship between force and motion is modeled using the mass-spring-damper model and describes how the system responds to external forces. The force sensor is used to measure the reaction force that occurs during contact between the robotic arm and the wall. Force measurement is used in the C-IC to adjust the motion of the arm in real-time, based on the modeled relationship between force and motion. This allows the robotic arm to respond to external forces in a stable and compliant manner, while still achieving the desired motion.

The mathematical model of the C-IC in  $s$  domain is given as:

$$\frac{P(s)}{F(s)} = \frac{1}{ms^2 + bs + k} \quad (22)$$

where  $m$ ,  $b$ , and  $k$  are the inertia, damping, and the stiffness coefficients, respectively.  $P$  is displacement in Cartesian space and  $F$  is a contact force.

In summary, the mass-spring-damper impedance model was used to obtain position, velocity, and acceleration based on the reaction force. Then, inverse kinematics were used to map from the Cartesian space to the joint space, and these joint variables were used as input for a PID with gravity compensation to control the robotic arm's movement.

The damping ratio ( $\zeta$ ) is an important parameter in identifying the dynamic behavior of a system, specifically how well the system oscillates and how quickly it returns to its equilibrium position. The damping ratio can be used to tune the coefficients of the C-IC, and the trial-and-error method is implemented in real-time to adjust these coefficients according to the damping ratio of the system. This allows for more precise control over the system's movement and behavior. The damping ratio was selected as 0.7, 2.2, and 11.2, whereas the natural frequency was 4.5, and the results for the x-y-z position were shown in Figure 11.

As shown in Figure 11 **Error! Reference source not found.**, the best result was obtained when the damping ratio was 11.2 and the natural frequency was 4.5.

By comparing the C-IC characteristic equation with the standard second-order characteristic equation, the coefficients of  $m$ ,  $b$ , and  $k$  can be calculated.

$$m = 1 \quad (23)$$

$$k = \omega_n^2 m = 4.5^2 \cdot 1 = 20.25 \quad (24)$$

$$b = 2m\omega_n\zeta = 2 \cdot 1 \cdot 4.5 \cdot 11.2 = 100.8 \quad (25)$$

The experimental study compares the performance of a C-IC system with that of a PID controller with gravity compensation for a robotic arm. In the experiment, a wall was placed 42 cm away from the robotic arm's x-axis, and the robotic arm was positioned at an initial position as shown in Figure 3. The x-y-z Cartesian reference trajectories were selected for the robotic arm to follow.

$$\begin{aligned} p_x(t) &= 34 - 0.041t^3 - 0.004t^4 - 0.0001t^5 \\ p_y(t) &= 0.082t^3 - 0.008t^4 - 0.0002t^5 \\ p_z(t) &= 44 - 0.026t^3 + 0.0026t^4 - 0.000007t^5 \end{aligned} \quad (29)$$

Figure 12 shows the time history responses of the results for x-y-z for both C-IC and PID with gravity compensation control, and Figure 13 displays the reaction force obtained during the contact of the wall.

#### 4. Experimental Results and Discussions

In Figure 11, three different damping ratios (0.7, 2.2, and 11.2) were examined for the same natural frequency of 4.5. With a damping ratio of 0.7, the system is underdamped, resulting in oscillations in the x and z positions. However, a damping ratio of 2.2 and 11.2 indicates an



overdamped system, in which no oscillations occur, as expected in the system response. The best x-y-z tracking performance was obtained when the damping ratio was 11.2.

The experimental study involved a robotic arm that was placed 42 cm away from a wall. The arm was programmed to make contact with the wall at the 5th second. The results of the experiment, using two different controllers, are shown in Figure 12. Both controllers were able to follow the trajectory until contact occurred on the x-axis. After contact, both controllers were able to follow the reference trajectory in the y-axis. However, the first controller experienced a slip in the z-axis and was unable to follow the trajectory, while the C-IC was able to follow the trajectory in all three axes (x, y, and z).

The results of the experimental study also showed that the reaction force generated during the contact was significantly reduced by using the C-IC as seen in Figure 13. The study showed that when using C-IC, the maximum reaction force generated during contact with the wall was 3.881 N. In contrast, when using the PID with gravity compensation, the maximum reaction force generated was 4.954 N. The results demonstrate that C-IC significantly reduced the reaction force generated during contact by 21.66%. The study has illustrated that the use of C-IC enables the robotic arm to effectively track the x-y-z reference trajectories, and also significantly decrease the force generated during contact.

In the face of uncertainties and disturbances, the performance of Cartesian impedance control can be impacted. These disturbances can result from various sources, such as unmodelled dynamics, measurement noise, or unexpected interactions with the environment. These uncertainties and disturbances can lead to the end effector deviating from its desired trajectory and affect the accuracy of the control.

One way to mitigate the effects of uncertainties and disturbances in Cartesian impedance control is to use robust control methods. These methods can be designed to handle the presence of disturbances and uncertainties and ensure that the control system remains stable and performs well in the face of these challenges. Another approach is to use an adaptive control method, which can adjust the impedance control law in real-time in response to changing conditions in the environment.

In summary, Cartesian impedance control can be affected by uncertainties and disturbances in its environment. However, these challenges can be addressed through the use of robust and adaptive control methods to ensure stable and accurate performance.

## **5. Conclusion**

This paper proposes a C-IC method for a 3 DOF robotic arm. This method has two loops, an inner PID with gravity compensation loop and an outer Cartesian impedance loop. The parameters of the PID with gravity compensation were calculated using a mathematical model of the robot dynamics obtained using the Matlab system identification toolbox. The transfer function of the robotic arm was estimated based on input-output data of the motor voltage and angular position of the links.

The closed-loop transfer function of the robotic arm was derived using the transfer function of each link coupled with the motor and the calculated PID coefficients. The pole placement method was used to calculate the PID coefficients for the first, second, and third links. The results

showed that the robotic arm successfully followed reference trajectories. In the C-IC, the relationship between force and motion was modeled using the mass-spring-damper model. The coefficients for the model were obtained using a trial-and-error method based on the damping ratio.

The paper also evaluated the performance of the two controllers on a robotic arm in contact with a wall. The results showed that the C-IC was able to efficiently follow the reference trajectory after contact with the wall. However, the PID with gravity compensation control failed to follow the reference and resulted in a shift in the z-axis.

The maximum force generated during contact was measured as 3.881 N and 4.954 N for the C-IC and PID with gravity compensation control, respectively. The C-IC resulted in a 21.66% reduction in contact force, providing less exposure of the robotic arm to reaction forces. An initial oscillation in the z-axis was observed in all experiments, which was attributed to the effect of gravity and gaps in the connections of the robotic arm.

### **Acknowledgments**

This work was supported by the Scientific Research Projects Coordination Unit of Bursa Technical University. Project number: 191N008.

### **Conflict of interest**

None

### **Nomenclature and assumptions**

$a_{i-1}$	transition along the x-axis
$d_i$	transition along the z-axis
$\alpha_{i-1}$	rotation about the x-axis
$\theta_i$	rotation about the z-axis
$m$	inertia coefficient of impedance
$d$	damping coefficient of impedance
$k$	stiffness coefficient of impedance
$\theta_1, \theta_2, \theta_3$	Angular position of the first, second and third link
$p_x, p_y, p_z$	x-y-z position of the end effector
$\varphi_1, \varphi_2, \varphi_3$	Auxiliary angles

$l_1, l_2, l_3$	Length of the first, second and third link
$K_P, K_I, K_D$	PID coefficients
$m_2, m_3$	weight of the second and third links
$h_2, h_3$	height of the center of gravity of the second and third links
$q_d$	desired angular position
$q$	angular position
$\dot{q}_d$	desired angular velocity
$\dot{q}$	angular velocity
$t$	Time

## References

1. Zeng, G. and Hemami, A., “An overview of robot force control”, *Robotica*, **15**(5), pp. 473–482 (1997).
2. Hogan, N., “Impedance Control: an Approach To Manipulation.”, *Proceedings of the American Control Conference*, **1**(March), pp. 304–313 (1984).
3. Ba, K., Yu, B., Zhu, Q., et al. “The position-based impedance control combined with compliance-eliminated and feedforward compensation for HDU of legged robot”, *J Franklin Inst*, **356**(16), pp. 9232–9253 (2019).
4. Nasir, K., Shauri, R. L. A., Salleh, N. M., et al. “Implementation of two-axis position-based impedance control with inverse kinematics solution for A 2-DOF robotic finger”, *International Journal of Engineering and Technology(UAE)*, **7**(3), pp. 10–14 (2018).
5. Dai, P., Lu, W., Le, K., et al. “Sliding Mode Impedance Control for contact intervention of an I-AUV: Simulation and experimental validation”, *Ocean Engineering*, **196**(June 2019) (2020).
6. Fargas-Marquès, A., Costa-Castelló, R., and Basañez, L., “Spatial Impedance Control in Coordinated Manipulation”, *IFAC Proceedings Volumes*, **33**(27), pp. 231–236 (2000).
7. Annamraju, S., Raj, S., Pediredla, V. K., et al. “Parameter determination technique for impedance control of interactive robots using transformation matrices”, *IFAC-PapersOnLine*, **53**(1), pp. 201–205 (2020).
8. Liang, L., Chen, Y., Liao, L., et al. “A novel impedance control method of rubber unstacking robot dealing with unpredictable and time-variable adhesion force”, *Robot Comput Integr Manuf*, **67**(August 2020), p. 102038 (2021).
9. Kang, S., Jin, M., and Chang, P. H., “A solution to the accuracy/robustness dilemma in impedance control”, *IEEE/ASME Transactions on Mechatronics*, **14**(3), pp. 282–294 (2009).

10. De Gea, J. and Kirchner, F., “Modelling and simulation of robot arm interaction forces using impedance control”, *IFAC Proceedings Volumes (IFAC-PapersOnline)*, **17**(1 PART 1) (2008).
11. Hanafusa, T. and Hunang, Q., “Control of position, attitude, force and moment of 6-DOF manipulator by impedance control”, *2018 15th International Conference on Control, Automation, Robotics and Vision, ICARCV 2018*, (1), pp. 274–279 (2018).
12. Tourajizadeh, H., Boomeri, V., Afshari, S., et al. “Design, modeling, and impedance control of a new in-pipe inspection robot equipped by a manipulator”, *Scientia Iranica*, **28**(1), pp. 355–370 (2021).
13. Winiarski, T., Sikora, J., Seredynski, D., et al. “DAIMM Simulation Platform for Dual-Arm Impedance Controlled Mobile Manipulation”, *2021 International Conference on Automation, Robotics and Applications, ICARA 2021*, pp. 180–184 (2021).
14. Ding, Y. and Thomas, U., “Improving Safety and Accuracy of Impedance Controlled Robot Manipulators with Proximity Perception and Proactive Impact Reactions”, (March), pp. 3816–3821 (2021).
15. Ramón, J. L., Pomares, J., and Felicetti, L., “Direct visual servoing and interaction control for a two-arms on-orbit servicing spacecraft”, *Acta Astronaut*, **192**(December 2021), pp. 368–378 (2022).
16. Palma, P., Seweryn, K., and Rybus, T., “Impedance Control Using Selected Compliant Prismatic Joint in a Free-Floating Space Manipulator”, *Aerospace*, **9**(8) (2022).
17. Wang, Y., Wu, H., and Mai, X., “An Impedance-Control Based Teleoperation System for Live-Line Maintenance Robot”, *J Phys Conf Ser*, **2025**(1), p. 012080 (2021).
18. Kana, S., Tee, K. P., and Campolo, D., “Human–Robot co-manipulation during surface tooling: A general framework based on impedance control, haptic rendering and discrete geometry”, *Robot Comput Integr Manuf*, **67**(July 2020), p. 102033 (2021).
19. Ochoa, H. and Cortesao, R., “Impedance Control Architecture for Robotic-Assisted Mold Polishing based on Human Demonstration”, *IEEE Transactions on Industrial Electronics*, **0046**(c), pp. 1–9 (2021).
20. Ochoa, H. and Cortesão, R., “Impedance control architecture for robotic-assisted micro-drilling tasks”, *J Manuf Process*, **67**(April), pp. 356–363 (2021).
21. Wu, Y., Lamon, E., Zhao, F., et al. “Unified Approach for Hybrid Motion Control of MOCA Based on Weighted Whole-Body Cartesian Impedance Formulation”, *IEEE Robot Autom Lett*, **6**(2), pp. 3505–3512 (2021).
22. Garate, V. R., Gholami, S., and Ajoudani, A., “A Scalable Framework for Multi-Robot”, **37**(6), pp. 1–15 (2021).
23. Zhang, H., Zhu, W., and Huang, Y., “A research on the control strategy of automatic charging robot for electric vehicles based on impedance control”, *J Phys Conf Ser*, **2303**(1) (2022).
24. Llanos, C. H., Munoz, D., and Pertuz Mendez, S. A., “Simulation and Implementation of Impedance Control in Robotic Hand”, (April) (2018).
25. Cheng, L. and Tavakoli, M., “Ultrasound image guidance and robot impedance control for beating-heart surgery”, *Control Eng Pract*, **81**(August), pp. 9–17 (2018).
26. Sharifi, M., Salarieh, H., Behzadipour, S., et al. “Tele-echography of moving organs using an Impedance-controlled telerobotic system”, *Mechatronics*, **45**, pp. 1339–1351 (2017).
27. Sharifi, M., Salarieh, H., Behzadipour, S., et al. “Beating-heart robotic surgery using bilateral impedance control: Theory and experiments”, *Biomed Signal Process Control*, **45**, pp. 256–266 (2018).

28. Akdoğan, E., Aktan, M. E., Koru, A. T., et al. “Hybrid impedance control of a robot manipulator for wrist and forearm rehabilitation: Performance analysis and clinical results”, *Mechatronics*, **49**(July 2017), pp. 77–91 (2018).
29. dos Santos, W. M. and Siqueira, A. A. G., “Optimal impedance via model predictive control for robot-aided rehabilitation”, *Control Eng Pract*, **93**(September), p. 104177 (2019).
30. Husmann, S., Kolkenbrock, M., Ketelhut, M., et al. “Fuzzy logic control of the support of a lightweight robot during rehabilitation”, *IFAC-PapersOnLine*, **52**(19), pp. 211–216 (2019).
31. Lau, J. Y., Liang, W., and Tan, K. K., “Enhanced robust impedance control of a constrained piezoelectric actuator-based surgical device”, *Sens Actuators A Phys*, **290**, pp. 97–106 (2019).
32. Denavit, J. and Hartenberg, R. S., “A Kinematic Notation for Lower Pair Mechanisms Based on Matrices”, *J Appl Mech*, **22**, pp. 215–221 (1955).
33. Spong, M. W., Hutchinson, S., and Vidyasagar, M., *Robot Modeling and Control*, Wiley New York (2006).
34. Tran, M. S., Le, N. B., Nguyen, V. T., et al. “Independent Joint Control System Design Method for Robot Motion Reconstruction”, *Lecture Notes in Electrical Engineering*, **465**, pp. 627–638 (2018).

### Biography

**Ayberk Beyhan** was born in February 1993, in Balıkesir, Turkey. He received his BSc degree in Mechatronic Engineering in Kocaeli University. He graduated with a Master’s degree in Mechatronic Engineering from Bursa Technical University. His MSc thesis related to force control on robotics. Currently he is a Ph.D. student in Bursa Technical University. His research areas are robotics, dynamic and kinematic modelling, and control.

**Nurettin Gökhan Adar** received his BSc degree in mechanical engineering from Sakarya University, Türkiye, in 2004, his MSc in mechanical engineering from İstanbul Technical University, Türkiye, in 2008, and his PhD degree in mechanical engineering from Sakarya University, Türkiye in 2016. He worked as a research assistant at Sakarya University during the years 2011-2018. He is currently an Assistant Professor in the Department of Mechatronics Engineering at Bursa Technical University, Bursa, Türkiye. In September 2022, he was successful in the Tübitak 1512 entrepreneurship program and founded Innosens Robot Teknolojileri. His research/teaching interests include robotics, control, mechanical system modeling, and image processing.

### Figures Captions

- Figure 1 3-DOF robotic arm with coordinate frame
- Figure 2 Joint variables in Cartesian space
- Figure 3 Experimental setup and the initial position of the robotic arm
- Figure 4 The block diagram of PID control
- Figure 5 The block diagram of the PID with Gravity Compensation Control
- Figure 6 The first link (a) motor voltage (input) (b) angular displacement (output)
- Figure 7 Results for the estimated different transfer functions of the first link
- Figure 8 Closed loop poles on s-planes with desired constraints
- Figure 9 The angular position of joints

Figure 10 The block diagram of the position-based impedance control

Figure 11 The results for C-IC according to the different damping ratio

Figure 12 The results for C-IC and PID with gravity compensation control

Figure 13 Reaction force

### Tables Captions

Table 1 D-H table

Table 2 The coefficients of a PID according to the Routh Hurwitz criteria

Table 3 PID coefficients for all links

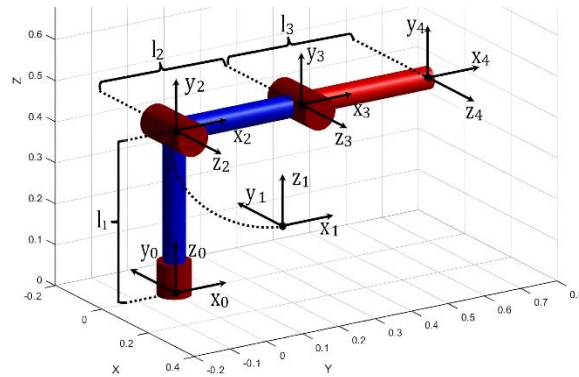


Figure 1 3-DOF robotic arm with coordinate frame

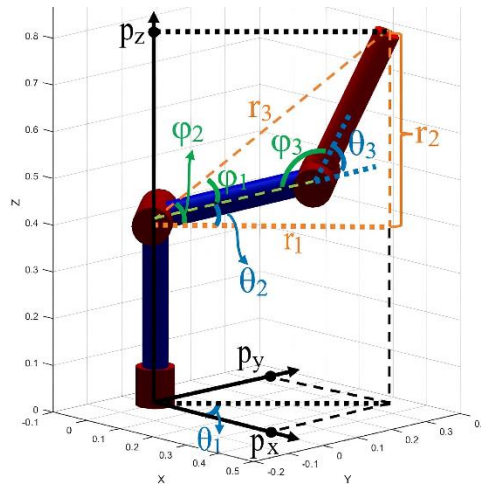


Figure 2 Joint variables in Cartesian space

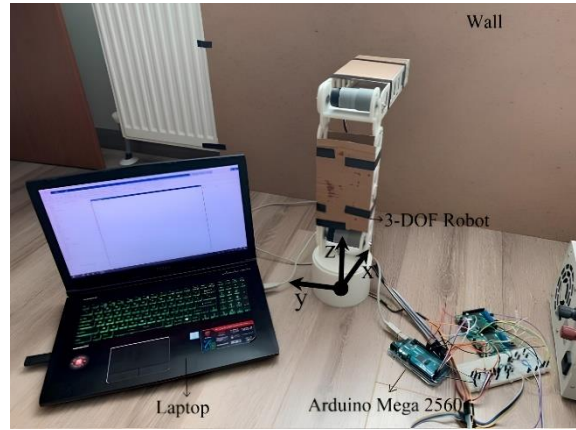


Figure 3 Experimental setup and the initial position of the robotic arm

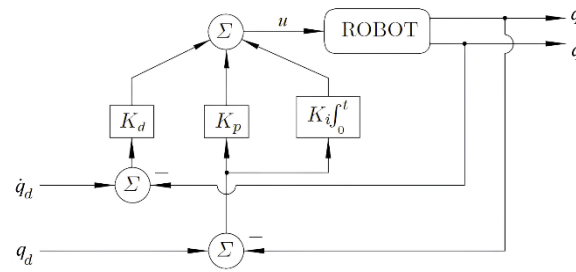


Figure 4 The block diagram of PID control

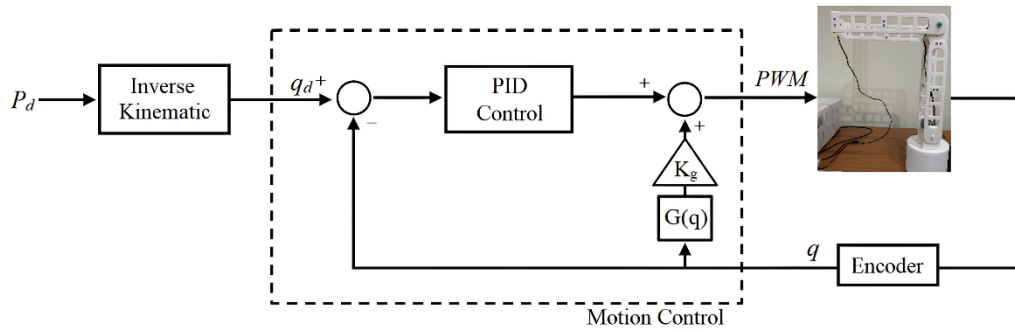


Figure 5 The block diagram of the PID with Gravity Compensation Control

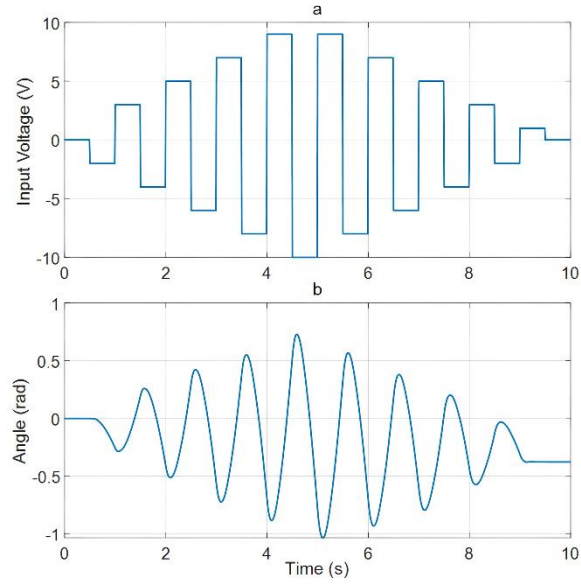


Figure 6 The first link (a) motor voltage (input) (b) angular displacement (output)

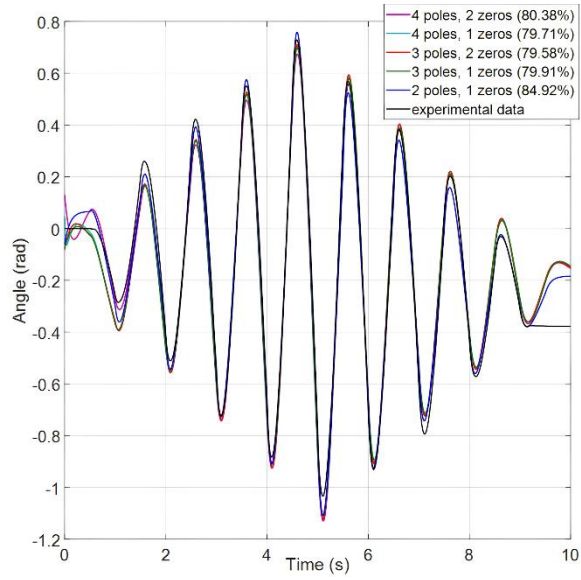


Figure 7 Results for the estimated different transfer functions of the first link



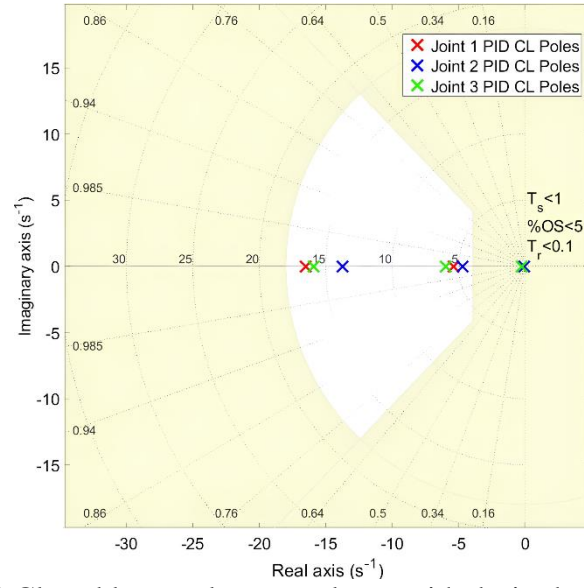


Figure 8 Closed loop poles on s-planes with desired constraints

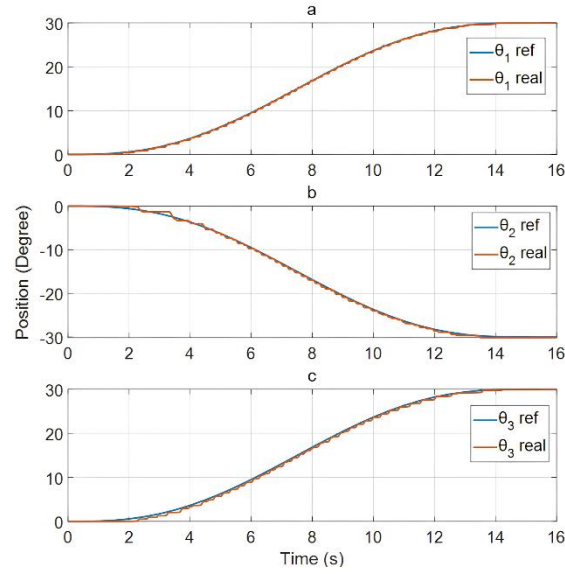


Figure 9 The angular position of joints

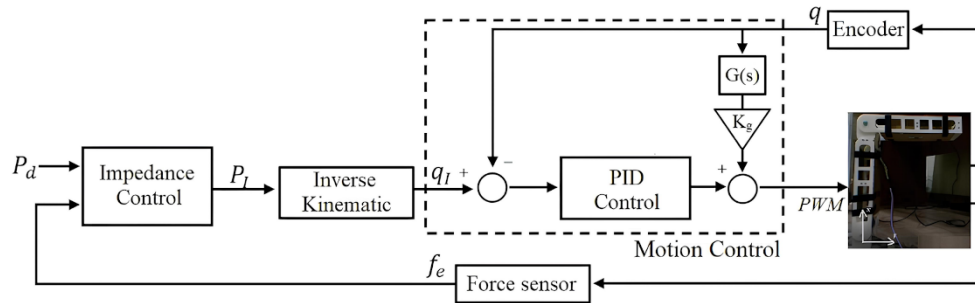


Figure 10 The block diagram of the position-based impedance control

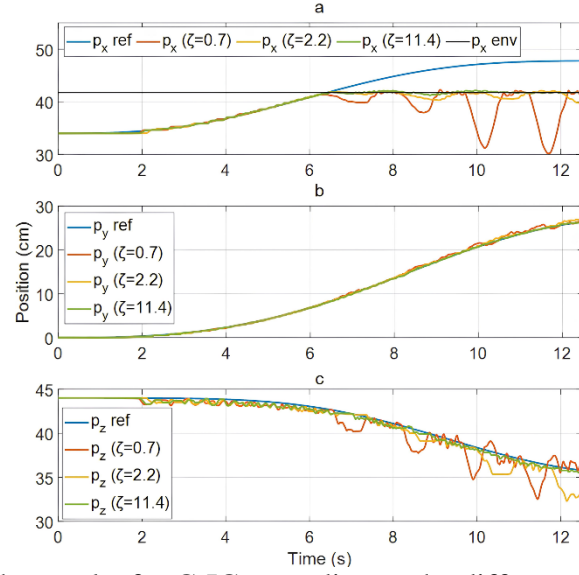


Figure 11 The results for C-IC according to the different damping ratio

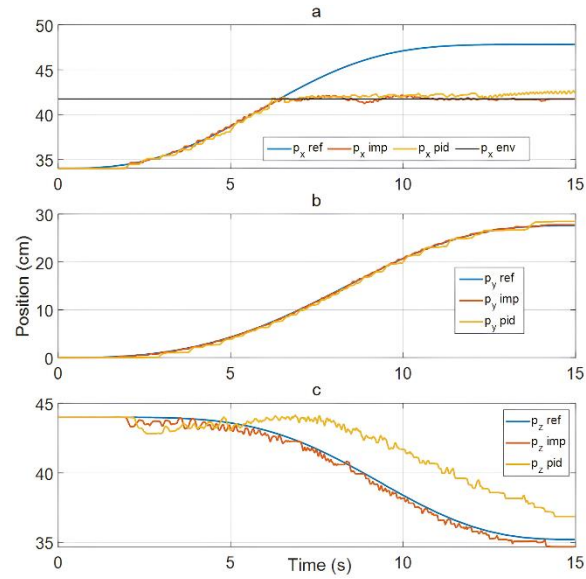


Figure 12 The results for C-IC and PID with gravity compensation control

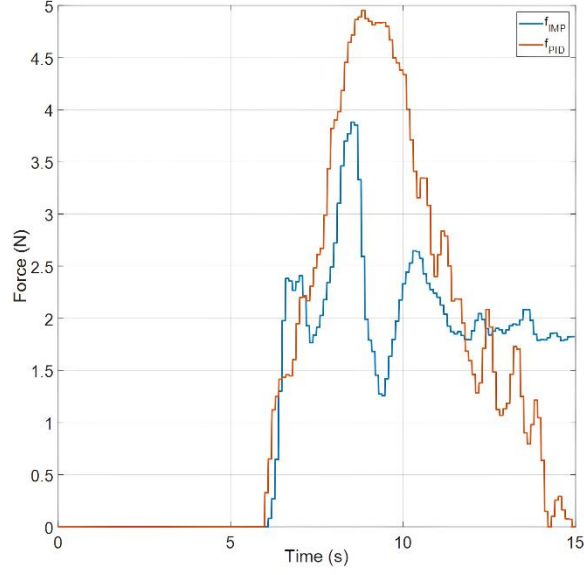


Figure 13 Reaction force

Table 1 D-H table

Coordinate Frames	$\alpha_{(i-1)}$	$a_{(i-1)}$	$d_i$	$\theta_i$
<b>1</b>	0	0	$L_1$	$\theta_1$
<b>2</b>	$\pi/2$	0	0	$\theta_2$
<b>3</b>	0	$l_2$	0	$\theta_3$
<b>4</b>	0	$l_3$	0	0

Table 2 The coefficients of a PID according to the Routh Hurwitz criteria

First link	$K_p < 32K_d + 64.67$
	$K_i < 32K_p, K_i > 0$
	$K_d < 6.67$
Second link	$K_p + 17.7K_i > -3.56$
	$K_d + 17.7K_p > -5$
	$K_i > 0$

	$K_d > -2.3$
	$K_i < 47.3K_d + 13.12$
Third link	$K_p < 47.3K_p + 71.24$
	$K_i > 0$
	$K_d < 5.88$

Table 3 PID coefficients for all links

	First link	Second link	Third link
$K_p$	14.4	24.2	10.2
$K_i$	3.2	4.96	2.5
$K_d$	1.8	4.32	1.02